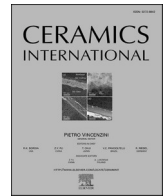




Contents lists available at ScienceDirect

Ceramics International

journal homepage: www.elsevier.com/locate/ceramint

Structure, impedance spectroscopy, and magnetic properties of nanostructured composites $(1-x)\text{CoFe}_2\text{O}_4-x\text{PbTiO}_3$

Bashir Abdulvakhidov^a, Sadyk Sadykov^a, Kamaludin Abdulvakhidov^{b,*}, Alexander Soldatov^b, Zhengyou Li^b, Yury Rusalev^b, Alexander Nazarenko^c, Pavel Plyaka^c, Salim Otajonov^d, Nurzod Yunusov^d, Maxamatjon Axmedov^d, Marina Vitchenko^e, Irina Mardasova^e

^a Dagestan State University, Gadgieva 43a, Makhachkala, 367000, Russia

^b Southern Federal University, Sladkova 178/24, Rostov-on-Don, 344090, Russia

^c Southern Scientific Center of the Russian Academy of Sciences, Chekhova 41, Rostov-on-Don, 344006, Russia

^d Fergana State University, Murabbiylar 19, Fergana, 100150, Uzbekistan

^e Don State Technical University, Gagarina 1, Rostov-on-Don, 344000, Russia

ARTICLE INFO

Handling Editor: Dr P. Vincenzini

Keywords:

Cobalt ferrite
Lead hexaferrite
Impedance spectroscopy
Magnetodielectric
Magnetoresistance
FORC analysis

ABSTRACT

The article presents a comprehensive investigation of the crystal structure, impedance spectra, magnetic, magnetodielectric, and magnetoresistive properties of $(1-x)\text{CoFe}_2\text{O}_4-x\text{PbTiO}_3$ composites with varying concentrations ($x = 0, 0.2, 0.4, \text{ and } 0.6$). The study also examines the effects of applying a uniaxial pressure of 1 GPa to the synthesized powders using Bridgman anvils. Our findings reveal that the synthesis of these composites results in the formation of an additional phase, lead hexaferrite $\text{PbFe}_{12}\text{O}_{19}$, which exhibits multiferroic properties. Additionally, the coherent scattering region of the components is significantly reduced after mechanical activation. Notably, the real part of the resistivity $\rho'(\omega)$ of nanostructured CoFe_2O_4 ceramics increases eightfold at $T = 240^\circ\text{C}$. The composites demonstrate significant magnetoresistance at room temperature, reaching up to 250%. The study also reveals that the signs of the magnetodielectric $MD(B)$ and magnetoresistive coefficient $MR(B)$ vary with the frequency of the measuring field for certain concentrations. Using the first-order reversal curve (FORC) method, it was observed that after nanostructuring CoFe_2O_4 through mechanical activation, the interaction field H_{11} shifts from ± 0.6 kOe to ± 0.8 kOe, while the coercive field H_c increases from 1.05 kOe to 5 kOe. Moreover, the two-dimensional FORC maps of the composites show increased complexity, due to the formation of additional magnetic phases.

1. Introduction

Manipulating the physical properties of polycrystalline functional materials through external influences, such as uniaxial pressure and shear deformation, during preparation offers significant advantages. However, structural changes induced by these external factors are often unaddressed, leading to incomplete and unreliable interpretations of the results. In this study, we utilize a combination of intense uniaxial force and shear deformation as external factors to shape and modify the physical properties of materials. This approach, known as “top-down” nanostructuring, is widely used to investigate the effects of mechanical activation on the properties of functional materials [1].

In our prior investigation [2], we conducted a comprehensive analysis of the $(1-x)\text{CoFe}_2\text{O}_4(\text{CFO})-x\text{PbTiO}_3(\text{PTO})$ composite. CFO, an

inverse spinel ferromagnetic material with semiconductor properties, has a magnetic phase transition temperature (T_m) ranging from 450°C to 527°C [3–6]. PTO, a classical ferroelectric, is a key component in various solid solutions [7,8].

Using X-ray diffraction and energy-dispersive analysis, we determined that during the synthesis of the $(1-x)\text{CFO}-x\text{PTO}$ composite, Ti^{4+} ions in PbTiO_3 are partially replaced by Fe^{3+} ions. This substitution results in a decrease in CFO concentration and the formation of an additional phase, lead hexaferrite ($\text{PbFe}_{12}\text{O}_{19}$, PFO), which exhibits both ferroelectric and magnetic properties [2,9]. Although the formation of PFO during the synthesis of the $(1-x)\text{CFO}-x\text{PTO}$ composite has been observed, it has often been reported without detailed structural or property analysis in the literature [10,11].

In this work, we present the results of studying the structural

* Corresponding author.

E-mail address: phys.kam@mail.ru (K. Abdulvakhidov).

<https://doi.org/10.1016/j.ceramint.2024.09.123>

Received 20 May 2024; Received in revised form 28 August 2024; Accepted 10 September 2024

Available online 11 September 2024

0272-8842/© 2024 Elsevier Ltd and Techna Group S.r.l. All rights are reserved, including those for text and data mining, AI training, and similar technologies.

parameters, impedance spectra, magnetic, magnetoresistive, and magnetodielectric properties of pre-synthesized $(1-x)\text{CFO}-x\text{PTO}$ composite samples with $x = 0, 0.2, 0.4,$ and 0.6 , which were nanostructured using the top-down method under a fixed pressure of 1 GPa. For comparison, the initial (non-nanostructured) samples were also investigated. In this study, the observed changes in physical properties are influenced not only by the presence of the PbTiO_3 component but also by additional factors such as structural defects—including point defects and dislocations—that are generated during mechanical activation.

It is well known that point defects, such as vacancies and interstitials, play a significant role in charge transport processes, especially in semiconductor microelectronics [12]. Controlling the concentration of these defects is essential for manipulating the electrical, magnetic, and structural properties of materials. In previous studies on ferroelectric relaxors, we demonstrated the potential to control parameters such as the degree of long-range chemical order (s), phase transition temperature (T_c), and characteristic Debye temperature (Θ) using mechanical activation at room temperature [13,14].

The physical properties of the synthesized macroscopic compositions are significantly influenced by particle size, which can range from several nanometers to several micrometers due to size reduction during mechanical activation and depends on both the applied pressure and the specific material properties. Larger particle sizes are formed due to agglomeration, a phenomenon driven by charge accumulation on particle surfaces resulting from the direct piezoelectric effect. This effect generates electric charges on the particle surfaces, promoting their attraction and subsequent agglomeration. When materials are broken down into smaller particles (dispersed), the number of surface atoms with broken bonds increases, leading to a higher specific surface area, which influences the material's physical properties. When particle sizes fall below 10 nm, quantum size effects become significant, altering the electronic and optical properties of the materials [15–20]. Therefore, investigating the impact of topological defects and particle size on the physical properties of functional materials is of both theoretical and practical importance.

The aim of this study is to examine the influence of topological defects and particle sizes on the physical properties of the nanostructured $(1-x)\text{CFO}-x\text{PTO}$ composite, including the additional PFO phase. Additionally, a comparative analysis was conducted to evaluate the physical properties of these nanostructured composites against their non-nanostructured (initial) forms.

2. Sample preparation and measuring equipment

For the solid-phase synthesis of CoFe_2O_4 , the oxides CoO and Fe_2O_3 ($\text{CoO} \geq 99.9\%$, $\text{Fe}_2\text{O}_3 \geq 99.9\%$, Sigma-Aldrich) were mixed in stoichiometric proportions. The mixture was ground in an agate mortar with ethanol for 2 h and then placed in a closed platinum crucible. Synthesis was performed in a high-temperature furnace at $1000\text{ }^\circ\text{C}$ for 4 h in the air. After cooling, the synthesized powder was ground again in the agate mortar for 1 h. X-ray diffraction (XRD) analysis confirmed the crystalline composition, with no impurity phases detected.

Lead titanate (PbTiO_3 , PTO) was synthesized using a solid-phase reaction. TiO_2 and PbO ($\text{TiO}_2 \geq 99.9\%$, $\text{PbO} \geq 99.9\%$, Sigma-Aldrich) were mixed in stoichiometric ratios, then ground in an agate mortar with ethanol for 1 h. The mixture was pressed into a tablet under 200 MPa and placed in a closed platinum crucible. Synthesis was performed in a high-temperature furnace at $900\text{ }^\circ\text{C}$ for 2 h in an air atmosphere. The furnace was then turned off, allowing the system to cool naturally to room temperature. The synthesized PTO was ground again in an agate mortar. Joint synthesis of CFO and PTO at various concentrations was performed at $900\text{ }^\circ\text{C}$ for 4 h.

Phase analysis of the synthesized samples was performed using an X-ray diffractometer (D2 Phaser, Bruker, Germany) with $\text{Cu K}\alpha$ radiation ($\lambda_1 = 1.5406\text{ \AA}$, $\lambda_2 = 1.5444\text{ \AA}$). The analysis utilized a step size of $\Delta 2\theta = 0.01^\circ$ and data collection time of $\tau = 0.1\text{ s}$, to identify the phases present

in the samples. The microstructure of the samples was examined using a scanning electron microscope (LEO EVO 40 XVP; Carl Zeiss AG, Germany). Magnetic properties were characterized at room temperature using a vibrating sample magnetometer (VSM, LakeShore 7404, USA). Magnetodielectric and magnetoresistive properties were measured in a constant magnetic induction field up to 2 T at room temperature, using a custom laboratory setup designed for these measurements. Impedance spectroscopy measurements were conducted from room temperature to 700 K using a PARSTAT 4000 system (Princeton Applied Research, USA).

To apply both high pressure and shear strain, the pre-synthesized powder was placed between Bridgman anvils, with the lower anvil rotating at 12.56 radians per hour to induce shear deformation. A pressure of 1 GPa was applied to the anvils for all concentrations. To minimize errors from pressure gradients, only the central part of the sample was analyzed. This process was repeated eight times for each concentration, and the resulting samples were ground in an agate mortar for 30 min.

For electrophysical measurements, ceramic disks with a diameter of 6 mm and a thickness of 1 mm were prepared by sintering the initial and nanostructured powders at $900\text{ }^\circ\text{C}$ for 4 h. Colloidal silver paste was applied to the disk surfaces as electrodes and then heated at $750\text{ }^\circ\text{C}$ for 10 min. The density and porosity of the ceramic samples were determined by hydrostatic weighing and are shown in Table 1.

As shown in Table 1, the density of the $(1-x)\text{CFO}-x\text{PTO}$ compositions changes non-monotonically following nanostructuring, while the porosity decreases significantly. The irregular variation in density may be attributed to the uncontrolled concentration of the PFO phase that forms during the composite synthesis. The unit cell volume of PFO at room temperature is 694.82 \AA^3 , which is significantly larger than the unit cell volumes of CFO and PTO, reported as 588.61 \AA^3 [21] and 65.3 \AA^3 [22], respectively. This difference in unit cell volume affects the overall density of the composite. The observed reduction in porosity following nanostructuring is likely due to the introduction of topological defects during mechanical activation. These defects reduce the activation energy required for diffusion processes during ceramic sintering, leading to decreased porosity.

3. Results and discussion

3.1. Microstructure

As shown in Fig. 1, the micrographs depict the $0.6\text{CFO}-0.4\text{PTO}$ powder in three stages: before mechanical activation (a), after mechanical activation (b), and after sintering to form the ceramic sample (c). Before mechanical activation, the powder particles are relatively uniform. After mechanical activation, these particles form conglomerates of smaller, fused particles with isometric shapes. During the subsequent sintering process, these conglomerates transform into larger crystallites with edge sizes reaching up to $5\text{ }\mu\text{m}$. Fig. 1 highlights crystallites corresponding to different phases: CFO (indicated by the middle arrow), PFO (indicated by the vertical arrow), and PTO (indicated by the lower horizontal arrow). In our previous study [2], energy-dispersive

Table 1

Density and porosity of $(1-x)\text{CFO}-x\text{PTO}$ compositions before and after nanostructuring.

Composition	Density (g/cm^3)	Porosity (%)
CFO	4.259	40.15
CFO (1 GPa)	5.108	16.44
0.8CFO-0.2PTO	5.116	25.34
0.8CFO-0.2PTO (1 GPa)	4.979	13.72
0.6CFO-0.4PTO	4.983	25.99
0.6CFO-0.4PTO (1 GPa)	4.957	21.16
0.4CFO-0.6PTO	5.372	27.50
0.4CFO-0.6PTO (1 GPa)	5.496	20.38

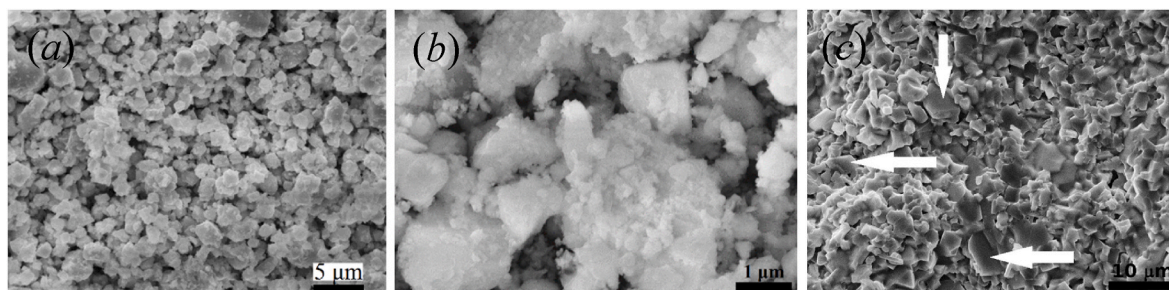


Fig. 1. Electron micrographs showing the synthesized powder (a), the mechanically activated powder (b), and the sintered ceramic sample of 0.6CFO-0.4PTO (c).

X-ray analysis (EDX), attached to an electron microscope, was employed to determine the elemental concentrations and identify grains with similar shapes, providing detailed compositional information.

Elemental analysis of some crystallites revealed the formation of solid solutions in addition to hexaferrite, with compositions ranging from $\text{PbFe}_{0.42}\text{Ti}_{0.86}\text{O}_{3.35}$ to $\text{PbFe}_{0.52}\text{Ti}_{0.95}\text{O}_{3.68}$ and from $\text{PbCo}_{1.55}\text{Fe}_{9.46}\text{Ti}_{1.21}\text{O}_{19.16}$ to $\text{PbCo}_{1.69}\text{Fe}_{8.24}\text{Ti}_{1.26}\text{O}_{17.57}$ [2]. The component indices in these formulas depend on the concentration of PTO and can vary even within a single ceramic sample. The Bragg peaks corresponding to these compositions were not detected in the X-ray diffraction patterns, likely due to their low concentration and, consequently, insufficient diffraction intensity. For the remaining composite powders, no significant differences were observed in the micrographs, and thus, they are not presented here.

3.2. X-ray diffraction analysis

Fig. 2 displays the X-ray diffraction patterns of the $(1-x)\text{CoFe}_2\text{O}_4-x\text{PbTiO}_3$ compositions with $x = 0.0, 0.2, 0.4,$ and 0.6 , both before and after nanostructuring. The patterns show the changes in phase and structural features due to nanostructuring. X-ray phase analysis of the compositions was performed using the Powder Cell 2.3 software package [23]. The Pseudo-Voigt 1 function, a standard peak shape function, was employed to approximate the diffraction peaks. The unit cell parameters were refined using the Rietveld method by adjusting atomic coordinates, site occupancies, and Debye-Waller isotropic

thermal factors [24,25]. The original X-ray diffraction patterns and the corresponding Rietveld refinement fitting results are provided in Appendix A.

A characteristic feature of the diffraction patterns for nanostructured compositions is the broadening of the diffraction profiles and an increased diffuse scattering background. This broadening indicates a reduction in crystallite size and the presence of microstrain or structural disorder. In Fig. 2(b), noticeable shifts of the Bragg peaks along the diffraction angle axis (2θ) are observed in the magnified section. These shifts are attributed to the formation of additional phases during composite synthesis and the presence of topological defects. However, the shifts do not follow a strict monotonic trend because the compositions exist in various metastable states, influenced by varying concentrations of structural defects and additional phases. For compositions with $x \neq 0.0$, peaks corresponding to CFO (space group $Fd3m$), PTO (space group $P4mm$), and PFO (space group $P6_3/mmc$, PDF # 41-1373) are observed [9].

Fig. 3 shows the dependence of the unit cell parameters of CFO, PTO, and PFO before and after nanostructuring.

As observed in Fig. 3(a), the unit cell parameter a of CFO increases with increasing x , while a^* decreases regardless of x . For PTO, the unit cell parameter c decreases as x increases, while the parameter a initially increases with x up to 0.4 and then decreases. The concentration point $x = 0.4$ is particularly noteworthy because, at this point, the minimum of a^* and the maximum of a are observed. The parameter c^* shows a consistent increase throughout the entire concentration range. Comparing the parameters c and c^* , the maximum change in c across the concentration range is $\Delta = 0.016 \text{ \AA}$, while the maximum change in c^* is $\Delta^* = 0.0016 \text{ \AA}$. The lattice parameter c^* increases after mechanical activation, which can be attributed to the topological defects generated during the nanostructuring process.

The change in the unit cell parameter a of PFO at the extreme concentration $x = 0.6$ is $\Delta_a = 0.045 \text{ \AA}$, and after nanostructuring, the change at the same point is $\Delta_{a^*} = 0.12 \text{ \AA}$. Meanwhile, the change in parameter c^* is negligible and falls within the margin of measurement error. Therefore, it can be concluded that under mechanical activation, the PFO unit cell expands in a plane perpendicular to the 6th-order symmetry axis.

The Williamson-Hall method is commonly used to estimate particle sizes in X-ray diffraction analysis. However, due to the overlap of diffraction profiles from various components in our compositions, this method is not applicable. To determine the sizes of coherent scattering regions (D), we use the Debye-Scherrer formula for the selected direction:

$$D = \frac{k\lambda}{\beta_{hkl} \cos \theta} \quad (1)$$

where k is a shape factor, λ is the wavelength of X-ray radiation, β_{hkl} is the full width at half maximum (FWHM) of the diffraction peak, and θ is the Bragg angle. It should be noted that the particle sizes estimated as D represent only the average sizes in the direction perpendicular to the hkl plane. In complex compositions, overlapping diffraction peaks of CFO

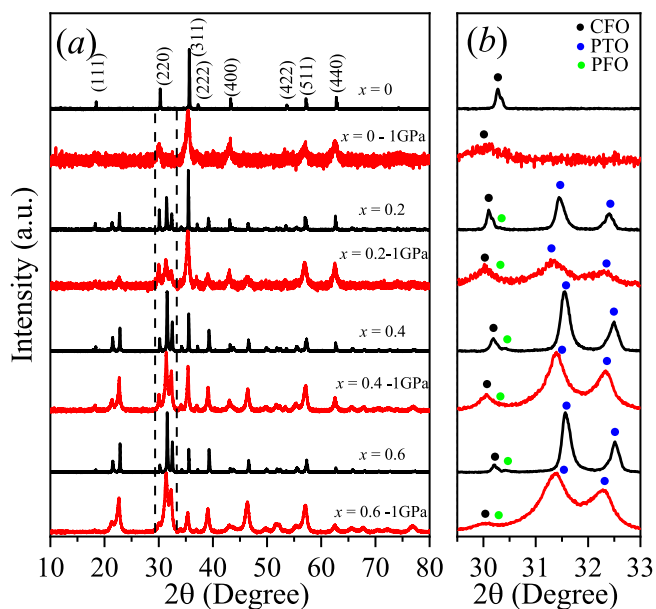


Fig. 2. Diffraction patterns of the compositions $(1-x)\text{CoFe}_2\text{O}_4-x\text{PbTiO}_3$ before and after mechanical activation (a) and their magnified sections (b).

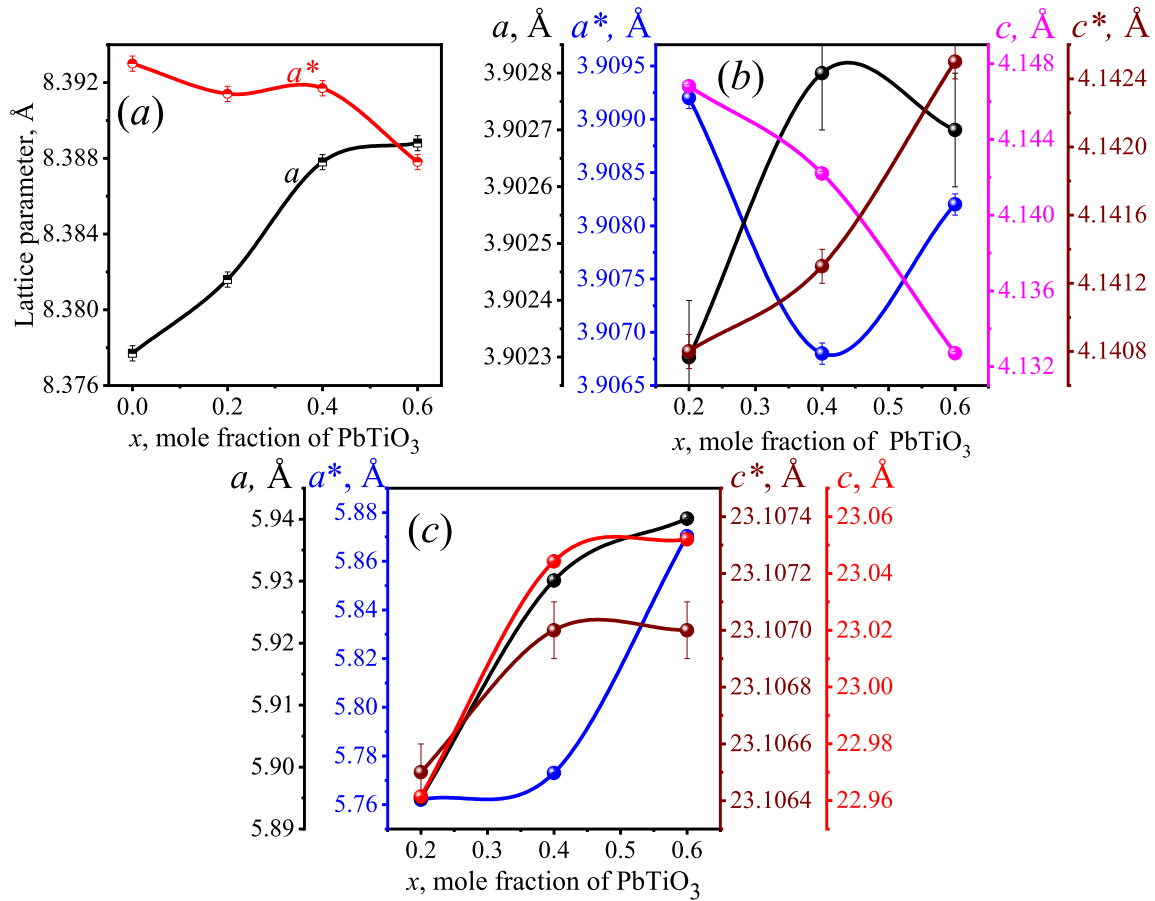


Fig. 3. Dependence of the lattice parameters for CoFe₂O₄ – (a), PbTiO₃ – (b), PbFe₁₂O₁₉ – (c). Parameters after mechanical activation are indicated with an asterisk.

with those of PTO and PFO complicate the analysis. Therefore, the estimation of *D* for CFO, PTO, and PFO was performed using single non-overlapping peaks: (220) for CFO, (101) for PTO, and (114) for PFO.

The results are presented in Table 2, which shows that nanostructuring by mechanical activation significantly decreases the *D* values for all composite components, as expected. As shown in Table 3, the *D* value of CFO before mechanical activation reaches its maximum at a

Table 2
Sizes of coherent scattering regions *D* for (1-*x*)CFO-*x*PTO components.

Composition - pressure	<i>D</i> , nm				ζ			
	<i>x</i>	<i>x</i>	<i>x</i>	<i>x</i>	<i>x</i>	<i>x</i>	<i>x</i>	<i>x</i>
	0.0	0.2	0.4	0.6	0.0	0.2	0.4	0.6
CFO	56	54.3	43	64.7	4.8	5 × 10 ⁻⁴	4.8	7.2
CFO - 1 GPa	6.8	15	18	26	2.1	1.7	1.4	1.2
PTO	-	39	37	39	-	7 × 10 ⁻⁴	4.8	9.6
PTO - 1 GPa	-	6.5	20	9.8	-	7.6	9.6	2.5
PFO	-	52	49	49	-	7.2	3.3	4 × 10 ⁻⁴
PFO - 1 GPa	-	9.4	26	15.7	-	2.2	1.3	1.7

Table 3

Dislocation densities (ρ_D) of composite components before and after mechanical activation.

Composition - pressure	ρ_D , cm ⁻²			
	<i>x</i> = 0.0	<i>x</i> = 0.2	<i>x</i> = 0.4	<i>x</i> = 0.6
CFO	9.6 × 10 ¹⁰	1.0 × 10 ¹¹	1.6 × 10 ¹¹	7.2 × 10 ¹⁰
CFO - 1 GPa	6.5 × 10 ¹²	1.3 × 10 ¹²	9.3 × 10 ¹¹	4.4 × 10 ¹¹
PTO	-	2.0 × 10 ¹¹	2.2 × 10 ¹¹	2.0 × 10 ¹¹
PTO - 1 GPa	-	7.1 × 10 ¹²	7.5 × 10 ¹¹	3.1 × 10 ¹²
PFO	-	1.1 × 10 ¹¹	1.2 × 10 ¹¹	1.2 × 10 ¹¹
PFO - 1 GPa	-	3.4 × 10 ¹²	4.4 × 10 ¹¹	1.1 × 10 ¹²

concentration of *x* = 0.6. After mechanical activation, *D* increases monotonically with increasing *x*, but remains significantly smaller than the values observed before mechanical activation. Before mechanical activation, the *D* values of the PTO and PFO components were nearly constant. After mechanical activation, the maximum *D* values for these components are observed at *x* = 0.4. At this concentration (*x* = 0.4), the microdeformation values ζ are minimal for nearly all components. Microdeformations were calculated using the formula:

$$\zeta = \frac{\beta_{hkl} \cos \theta}{4} \quad (2)$$

where β_{hkl} is the width at half maximum of the Bragg profile and θ is the diffraction angle.

The results presented in Table 2 show that nanostructuring leads to an increase in microdeformations by one to two orders of magnitude, depending on the composition concentration.

Next, the dislocation densities, ρ_D , representing topological defects,

were calculated from the D values using the formula:

$$\rho_D = 3nD^{-2} \quad (3)$$

where $n = 1$, under the assumption that grain boundaries form a three-dimensional dislocation network [26]. The results are summarized in Table 3.

As shown in Table 3, the dislocation densities ρ_D of each component are relatively consistent, showing only minor variations. The sizes of D are similarly consistent across different components, with only slight differences that can be considered negligible. After nanostructuring, as expected, the value of D decreases, while the dislocation density ρ_D increases across all concentrations.

3.3. Impedance spectroscopy

Impedance spectroscopy, a relaxation method, is widely used to analyze the behavior of parameters in nonlinear electrical circuit elements under external influences [27,28]. These parameters include resistance R_{gb} , R_g as well as capacitance C_{gb} and C_g , which represent the grain boundaries and grain volume of samples, respectively. These samples typically behave as ceramic capacitors, and temperature often serves as an external influence.

For a more accurate comparative analysis, we used resistivity values, denoted as ρ^* , instead of the complex impedance Z^* :

$$\rho^* = \rho' - j\rho'' \quad (4)$$

where ρ' represents the active component, ρ'' represents the reactive component of specific resistance, with j being the imaginary unit. Since clear dependencies for all compositions were observed only in the temperature range of 150–220 °C, we limited our analysis to this specific range.

Figs. 4 and 5 show the dependencies of $\rho'(\omega)$, $\rho''(\omega)$ and $\rho''(\rho')$ for $(1-x)$ CoFe₂O₄- x PbTiO₃. Within the frequency range of 10⁴–10⁷ Hz, the $\rho'(\omega)$ dependencies of CFO converge into a single line as the temperature increases. Meanwhile, $\rho''(\omega)$ is suppressed, showing weak relaxation behavior characterized by two maxima (Fig. 4(a')). The low-frequency maximum corresponds to grain boundary conductivity, while the high-frequency maximum corresponds to grain volume conductivity.

Nanostructured CFO is characterized by a decrease in $\rho'(\omega)$ with increasing temperature, starting from approximately 10² Hz, and the graphs merge into a single line at approximately 10⁶ Hz (see Fig. 4(b)). Beyond this frequency, only the constant component of the measuring field actively influences charge transport [29,30]. Each resistivity curve in Nyquist coordinates (see Fig. 4(a'')) comprises two arcs, representing the contributions from grain boundaries and grain volumes. Although the effects due to grain boundaries and volumes are not explicitly highlighted in Fig. 4(b') and 4(b''), they become apparent when each curve is considered individually and will be discussed in detail for each composition in Fig. 7.

A comparison of the real part ($\rho'(\omega)$) at $T = 150$ °C, used as a reference point, shows that after nanostructuring, this parameter increases by more than eight times. This suggests the potential for targeted control of

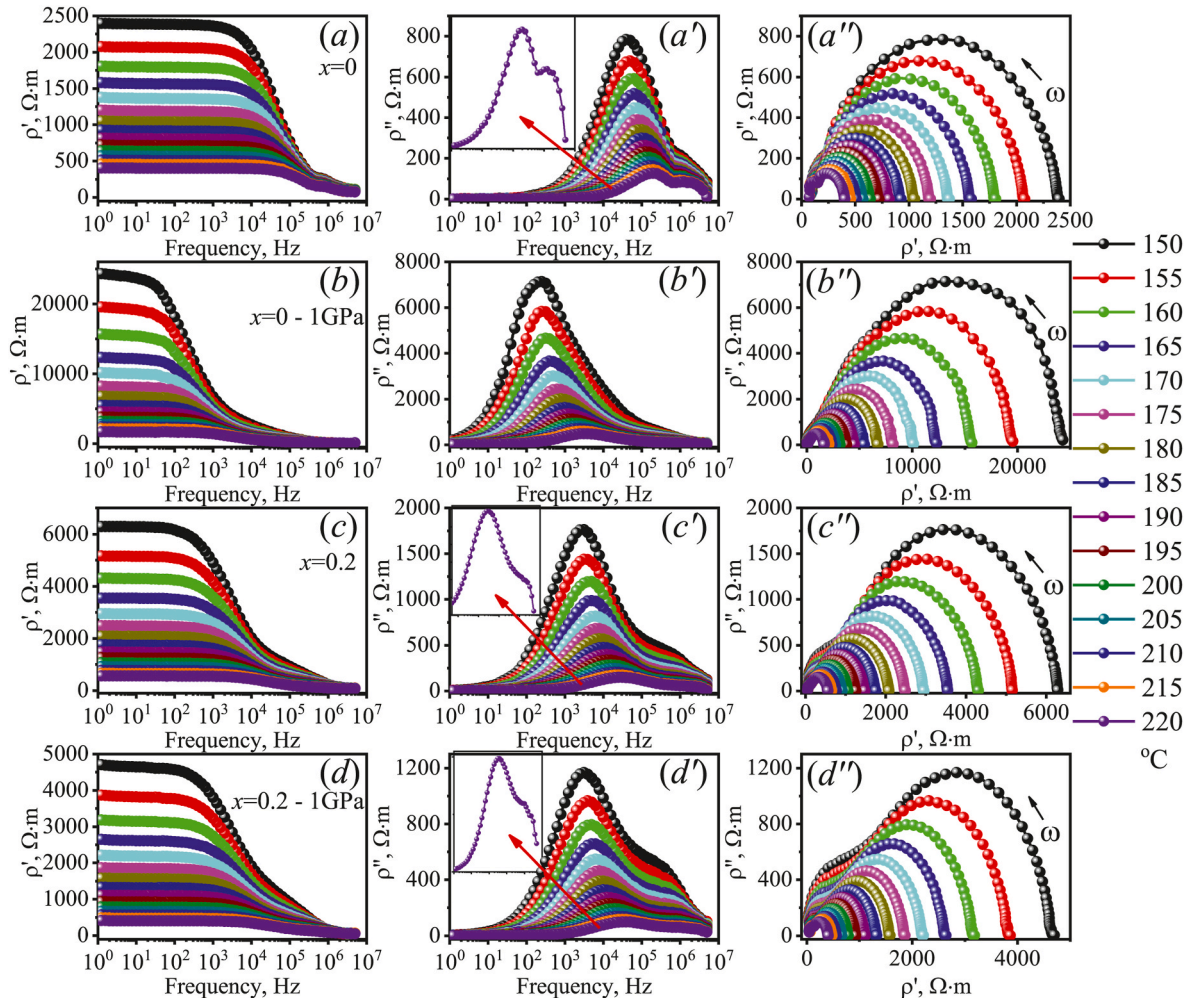


Fig. 4. Impedance spectroscopy of CFO before (a, a', a'') and after (b, b', b'') mechanical activation, as well as 0.8CFO-0.2PbTiO₃ before (c, c', c'') and after (d, d', d'') mechanical activation.

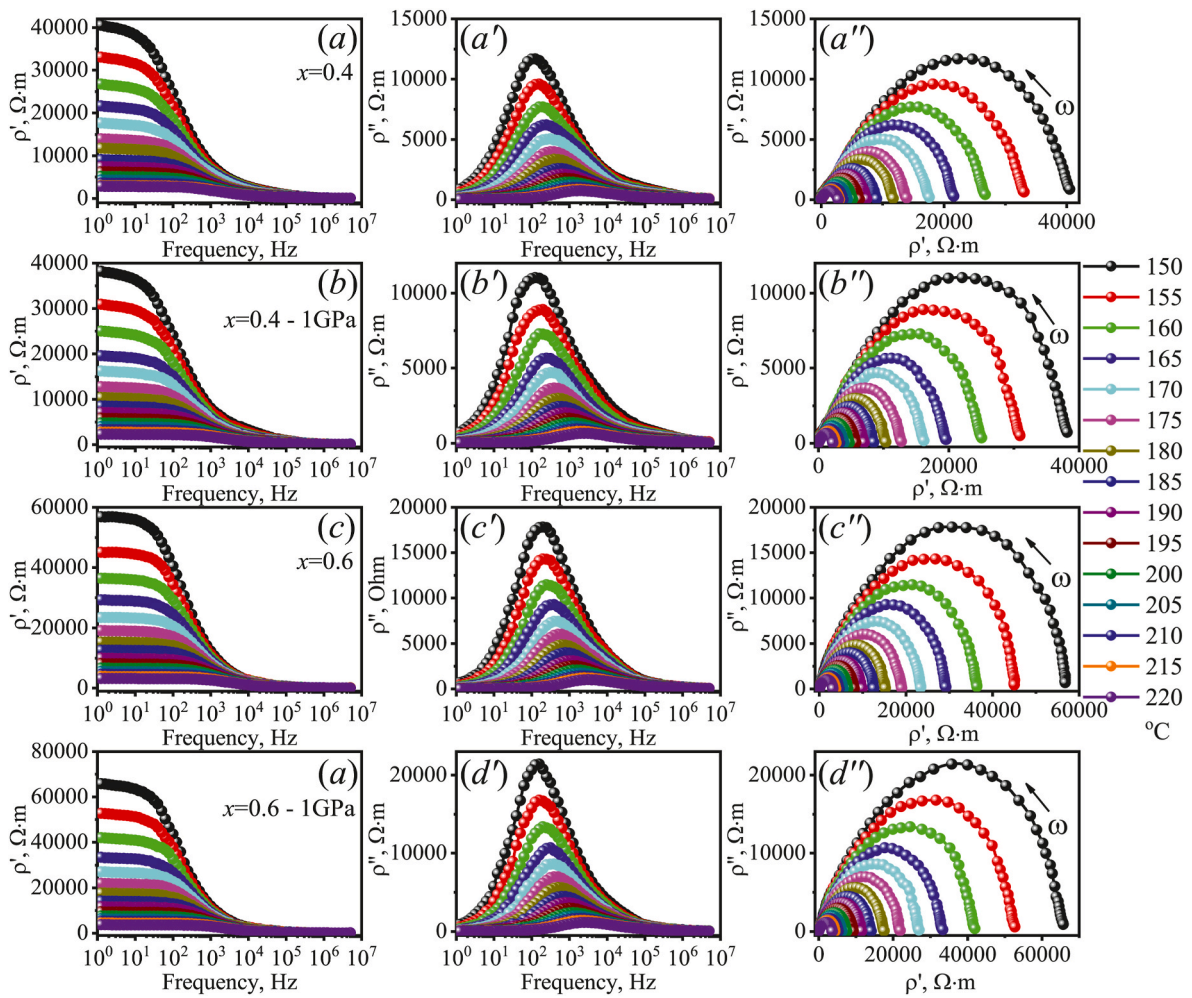


Fig. 5. Impedance spectroscopy of 0.6CF0–0.4PTO before (a, a', a'') and after (b, b', b'') mechanical activation, as well as 0.4CF0–0.6PTO before (c, c', c'') and after (d, d', d'') mechanical activation.

$\rho'(\omega)$, indicating that appropriate mechanical activation pressures should be selected to achieve the desired effects.

Both 0.8CF0–0.2PTO compositions, before and after

nanostructuring, exhibit similar graph behaviors: a decline in $\rho'(\omega)$ beginning in the range of $10^2 - 10^3$, with the curves merging into a single line at approximately 10^6 Hz (see Fig. 4(c, d)). The plots of $\rho''(\omega)$

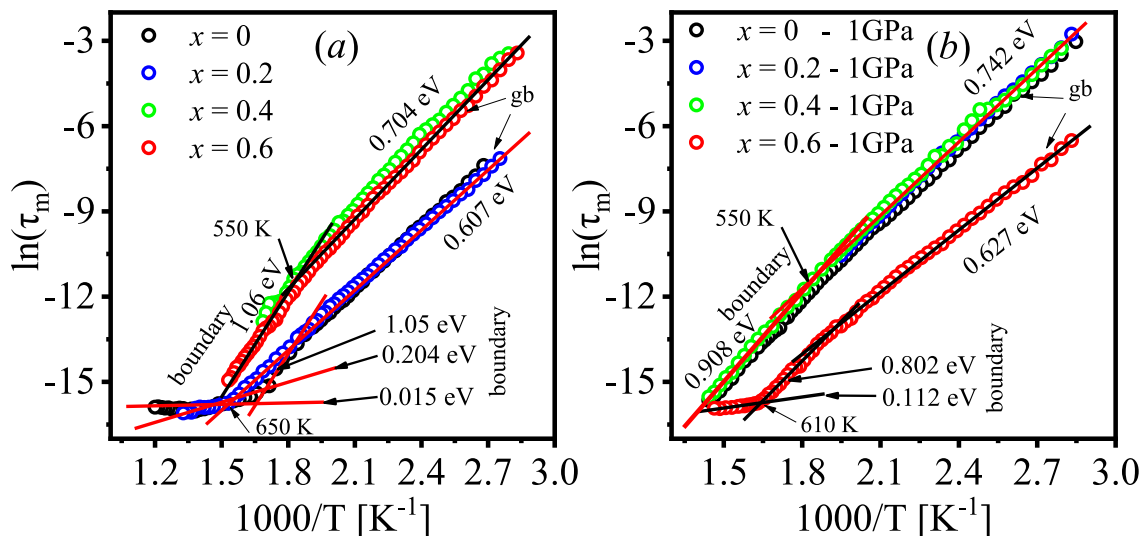


Fig. 6. Temperature dependencies of $\ln(\tau_m)$ for (1-x)CF0–xPTO compositions: x = 0.0, 0.2, 0.4, 0.6 (a) for initial samples, (b) for nanostructured samples.

display two maxima, with the second one being less pronounced (Fig. 4 (c', d')). The graphs in Nyquist coordinates (Fig. 4(c'', d'')) show a slight decrease in the real part of the resistivity after nanostructuring.

With a further increase in the concentration of PbTiO_3 , as shown in Fig. 5(a, b, c, d), the onset of the decline in the real part of impedance, $\rho'(\omega)$, shifts to lower frequencies, and no wide plateau is observed. The decline begins in the frequency range of 10–100 Hz, and the curves merge into a single line at approximately 10^4 Hz. Beyond this frequency range, the transport properties are primarily influenced by the DC component of the measuring field [29,30]. The maxima of the imaginary part, $\rho''(\omega)$, also shift to lower frequencies, and the dependencies exhibit an almost symmetrical shape (Fig. 5(a', b', c', d')). Although the effects caused by the grain boundaries and volumetric parts of individual phases are not distinguished in the Nyquist plots $\rho''(\rho')$ (see Fig. 5(a'', b'', d'')), they become apparent when examined separately in other graphs. The centers of the arcs are located above the real part of the impedance axis, $\rho'(\omega)$, indicating that the relaxation observed in these compositions is a non-Debye and thermally activated process. A comparison of the ρ' data for mechanically activated compositions reveals that the value at

the reference point increases with increasing x (see Figs. 5 and 6).

Next, we determined the activation energy E_a of each composition based on experimental data. The relaxation time τ_m corresponding to the maximum peak was calculated using the Arrhenius equation:

$$\tau_m = \tau_0 \exp(E_a / k_B T) \quad (5)$$

where τ_0 is the pre-exponential factor, E_a is the activation energy, k_B is the Boltzmann constant, and T is the absolute temperature in Kelvin.

In Fig. 6, kinks are observed in the plots of $\ln(\tau_m)$ versus inverse temperature ($1/T$), which separate the temperature intervals where either the grain boundaries or the bulk parts of the grains predominantly influence charge transport. Mechanical activation slightly increases the activation energy associated with the grain boundaries. This increase can be attributed to the heightened scattering of charge carriers at amorphous grain boundaries, which are thicker and more irregular than those in non-mechanically activated compositions. The plateau observed in the high-temperature region reflects the conductivity of the bulk crystallite regions [31,32]. After nanostructuring, this plateau decreases and shifts to higher temperatures and lower frequencies. This

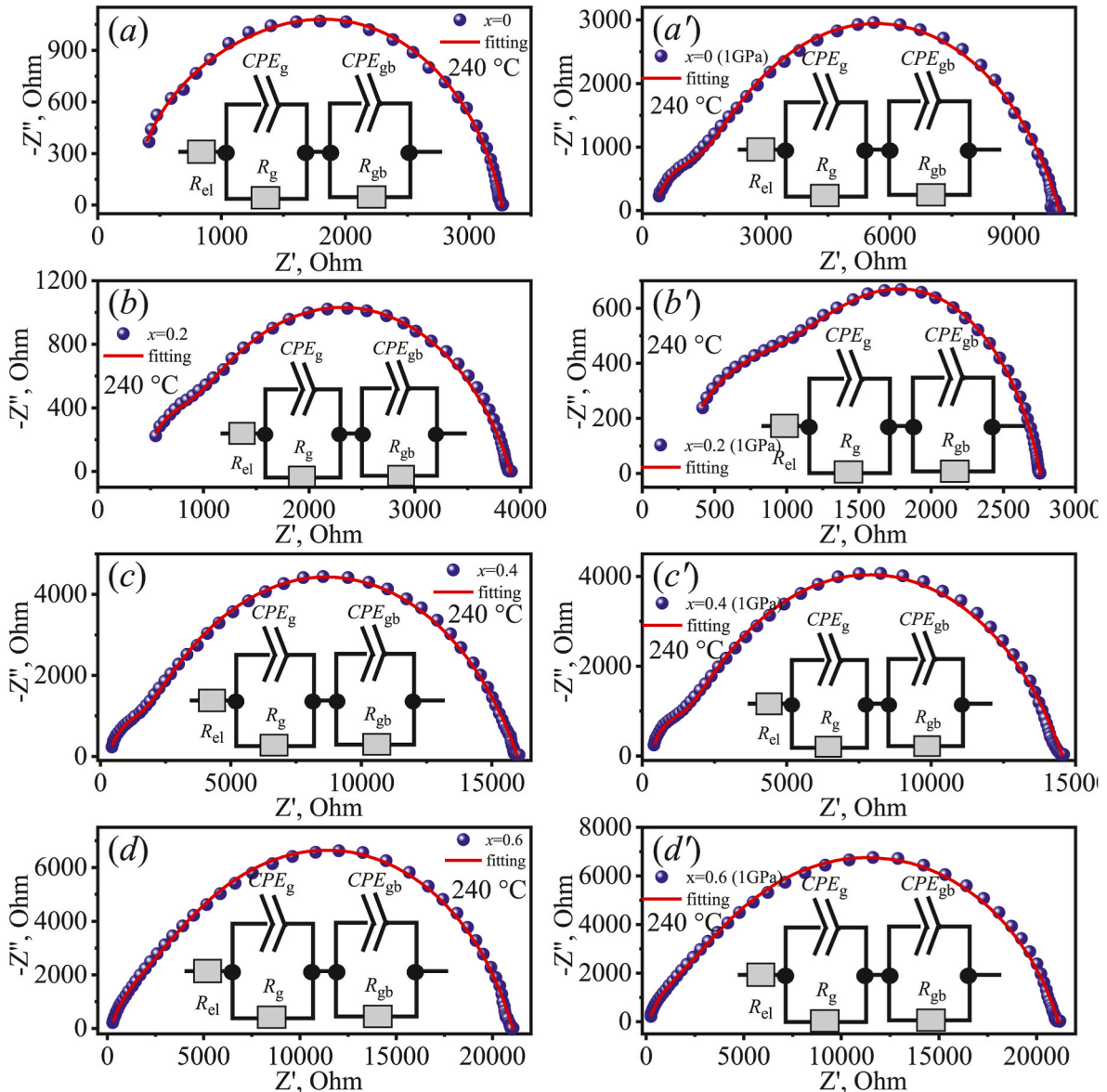


Fig. 7. Experimental and theoretical curves, along with the corresponding equivalent circuits for the initial compositions: CFO (a), 0.8CFO–0.2PTO (b), 0.6CFO–0.4PTO (c), 0.4CFO–0.6PTO (d); and the corresponding nanostructured compositions: (a'), (b'), (c'), (d').

trend is consistent with the behavior of $\rho''(\omega)$ as illustrated in Fig. 5(a, b, c, d).

The dissipative properties related to charge transfer in polycrystalline materials depend on the parameters of the grain boundaries and the bulk volume of the crystallites. These parameters are determined using models known as equivalent circuits. Such parameters include the resistance (R_g , R_{gb}) and capacitance (C_g , C_{gb}) of the crystallite volumes and their boundaries.

To perform a quantitative analysis of the impedance for each sample, we used the EIS Spectrum Analyzer software. The equivalent circuits for the samples, both before and after nanostructuring, were selected as shown in the insets of Fig. 7. Notably, the equivalent circuits for all compositions remained consistent throughout the analysis. A temperature of $T = 240^\circ\text{C}$ was chosen for the comparative analysis because it is outside the range of phase transitions in the initial components, allowing for optimal differentiation of resistance contributions in the $Z''(Z')$ graph. These graphs effectively distinguish the contributions of resistance from the grain boundaries and the bulk grain regions. The experimental curves obtained indicate the presence of two or more relaxation processes. Notably, the R_{el} values of the electrodes, which exhibit ohmic resistance, were not considered in our analysis.

Fig. 8 shows the temperature dependencies of the parameters of the equivalent circuits. The resistances of the bulk, R_g , and grain boundaries, R_{gb} , decrease exponentially with increasing temperature for all compositions. This decrease is attributed to the scattering of charge carriers at grain boundaries, defects, and the thermal vibrations of the crystal lattice.

Comparing R_{gb} and R_g at the fixed temperature of $T = 180^\circ\text{C}$, showed that for concentrations $x = 0.0$ and 0.6 , R_{gb} is less than R_g . However, after nanostructuring, R_{gb} exceeds R_g for all compositions. This shift is due to intensified diffusion processes during the sintering of

ceramics after mechanical activation, which increases the thickness of the amorphous layer. This increase is caused by the migration of nonequilibrium defects to the grain surfaces [31,32].

The capacitance of each composition, denoted as C_g (or CPE_g when considering the constant phase element), increases with rising temperature. Depending on the value of x , the capacitance reaches its maximum within the temperature range of $T = 150\text{--}300^\circ\text{C}$. The increase in C_g and C_{gb} (CPE_g) is due to the increased mobility of charge carriers trapped in defects within the crystal lattice, including at grain boundaries, as well as the thermal expansion of the grain volume. Maxwell-Wagner polarization begins at temperatures above $T = 150^\circ\text{C}$. Since the bulk of the grains is less defective than the amorphous grain boundaries, the maxima in the $C_{gb}(T)$ dependence for the grain boundaries appear at higher temperatures.

It is important to note that CPE is a frequency-dependent parameter. Its impedance is given by:

$$Z_{CPE} = A^{-1}(j\omega)^{-n} \quad (6)$$

where A is the proportionality coefficient, and n is the exponential parameter indicating the phase deviation, with $0 \leq |n| \leq 1$. When n is an integer, the CPE element represents classical elements with lumped parameters such as capacitance (C), resistance (R) and inductance (L) [33].

3.4. Magnetic properties

A common method for studying the magnetic properties of materials is to construct the primary magnetic hysteresis loop $M(H)$ (see Fig. 9(a-d) and Fig. 10(a-d)) and calculate integral parameters such as coercive force (H_c), remanent magnetization (M_r), and saturation magnetization

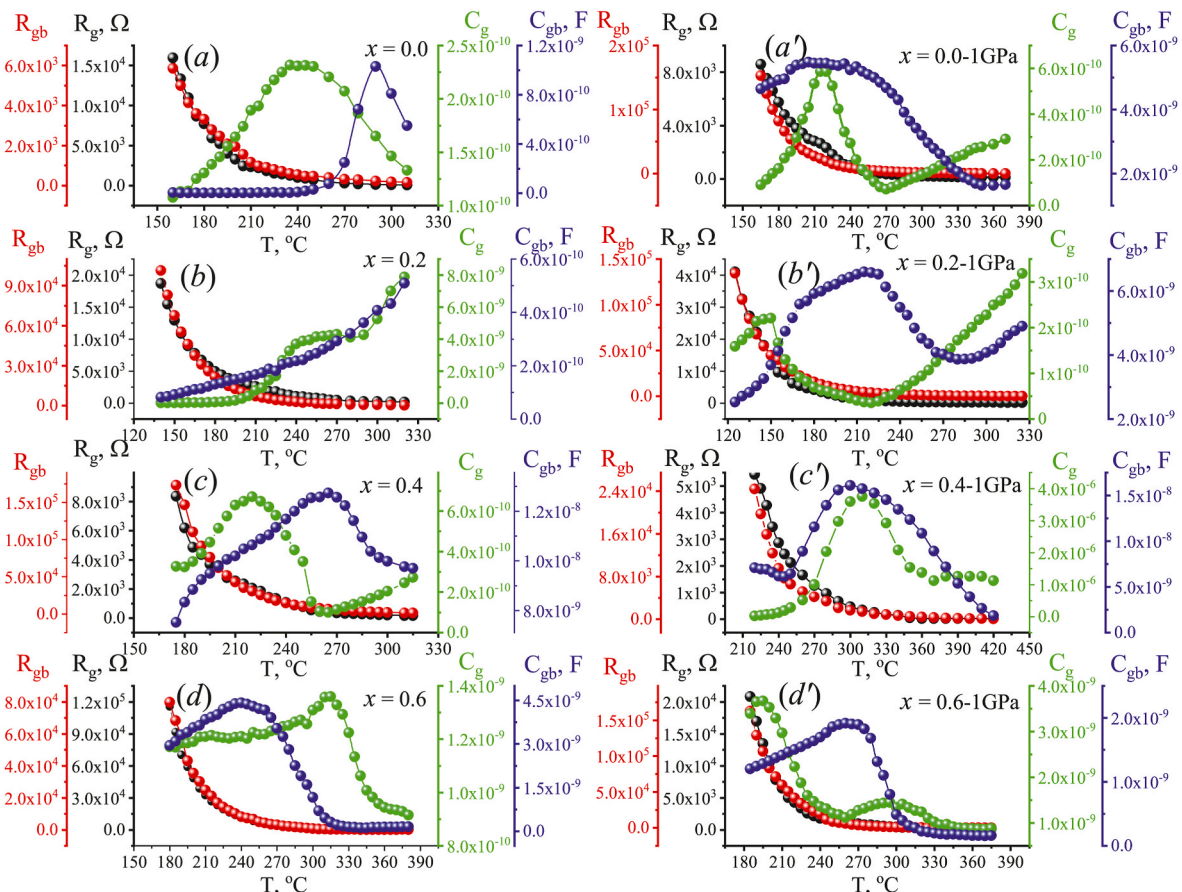


Fig. 8. Temperature dependencies of the parameters of the equivalent circuits before nanostructuring (a, b, c, d) and after nanostructuring (a', b', c', d').

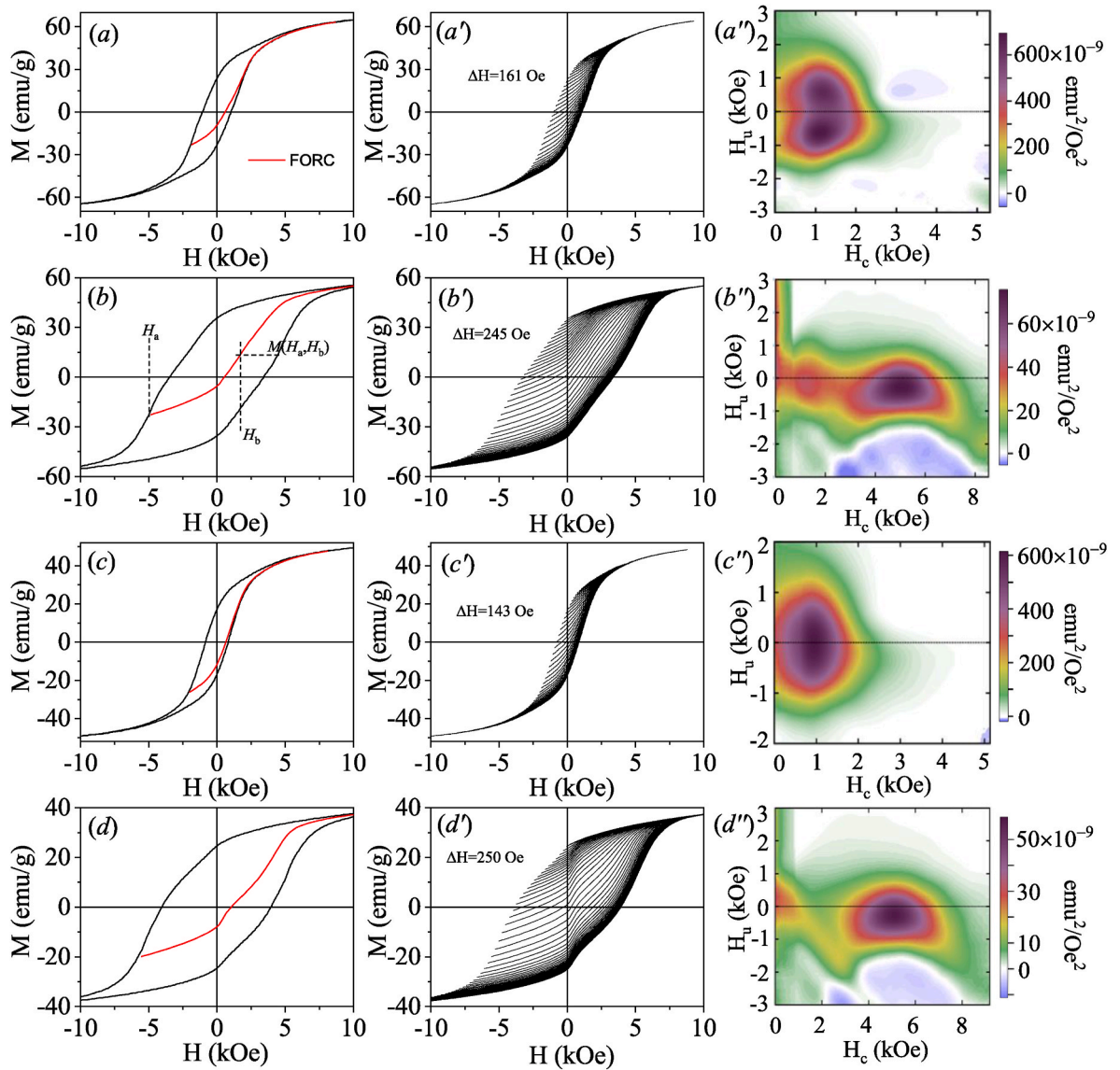


Fig. 9. Hysteresis loops, FORC diagrams, and two-dimensional distribution maps for different conditions: (a), (a'), (a'') - $x = 0.0$; (b), (b'), (b'') - $x = 0.0$, 1 GPa; (c), (c'), (c'') - $x = 0.2$; (d), (d'), (d'') - $x = 0.2$, 1 GPa.

(M_s). However, in heterogeneous or multi-phase magnetic materials, the $M(H)$ loop represents an overall property, which can obscure the contributions of individual phases. Therefore, it is important to explore other methods to clarify these contributions.

The FORC (First Order Reversal Curves) method, based on the Preisach model [34], has recently been widely used to study the properties of magnetic materials and composites.

The Preisach model describes a magnetic material as a network of small, independently acting, and parallel-connected domains. The magnetic behavior of the material is characterized by a combination of simple hysteresis loops, known as hysterons. Any hysteresis loop containing multiple magnetic phases can be represented as a set of hysterons with various Preisach distribution functions, denoted as $P(H_a, H_b)$. The Preisach function, $P(H_a, H_b)$, depends on the switching field H_a (often the coercive force in bistable loops) and the interaction field H_b (which determines the position of the hysteron in the diagram).

FORC diagrams can reveal the distribution of coercive forces and magnetic interactions in compositions with different magnetic phases [35–37]. Therefore, they are useful for identifying magnetic phases. Additionally, this method is effective for investigating the ‘internal’ magnetic structure of single-phase compositions [38].

In this study, measurement results were processed using the VARI-FORC program [39], and the FORC diagram was constructed using the following steps: 1. The sample was magnetized to saturation at a saturation field H_s of approximately 17 kOe. 2. Next, the external magnetic field was reduced to a reversible field $H_a = H_s - \Delta H \times n$, where ΔH varied for each curve, and n represents the curve number. 3. Finally, the magnetic field was increased back to the saturation field H_s . The optimal step ΔH used to shift H_a was determined for each composition and is shown in each figure.

Fig. 9(b) shows a single step of the FORC curve, while Fig. 9(a', b', c', d') and 10(a', b', c', d') display 100 FORC curves for each composition. The next step involved converting the coordinates from H_a and H_b to $H_c = (H_b - H_a)/2$ and $H_u = (H_b + H_a)/2$. This coordinate transformation was originally developed by Mayergoz [40]. The FORC distribution is represented as a mixed second derivative of the magnetization:

$$\rho(H_u, H_c) = -\partial^2 M(H_u, H_c) / \partial H_u \partial H_c \quad (7)$$

where H_u represents the distribution of interaction fields within spin ensembles, and H_c represents the distribution of switching fields in local magnetization regions.

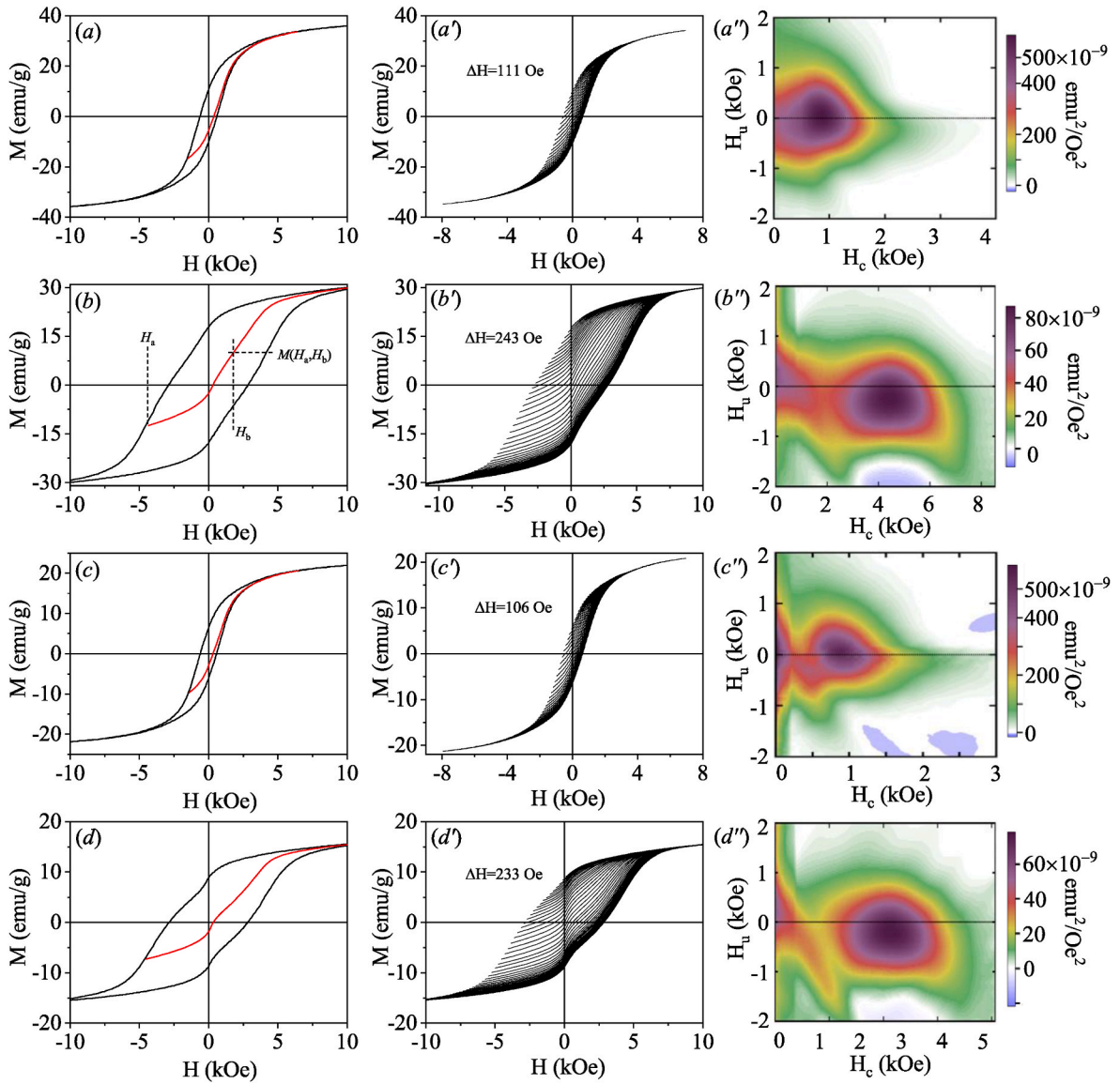


Fig. 10. Hysteresis loops, FORC diagrams, and two-dimensional distribution maps for different conditions: (a), (a'), (a'') - $x = 0.4$; (b), (b'), (b'') - $x = 0.4$, 1 GPa; (c), (c'), (c'') - $x = 0.6$; (d), (d'), (d'') - $x = 0.6$, 1 GPa.

Fig. 9(a-d and a'-d') and 10(a-d and a'-d') depict classic hysteresis loops and FORC curves for four concentrations, both before and after nanostructuring. Two-dimensional distribution maps of the FORC diagrams for the same compositions are shown in Fig. 9(a''-d'') and 10(a''-d'').

The macrodomain CoFe_2O_4 (as shown in Fig. 9(a'')) is characterized by the FORC diagram with a switching field $H_c = 1.05$ kOe and an interaction field $H_u = \pm 0.6$ kOe, which exhibits two humps symmetrically positioned relative to the zero line. This distribution of humps indicates the presence of magnetostatic interactions. For the macrodomain $0.8\text{CoFe}_2\text{O}_4-0.2\text{PbTiO}_3$ (as shown in Fig. 9(c'')), a stretched region along $H_u = \pm 0.8$ kOe is observed, with the center of the hump at $H_c = 1.05$ kOe. Notably, at $x = 0.2$, the formation of the PFO hexaferrite occurs, resulting in the sample comprising at least three phases. Two of these phases exhibit magnetic properties, while the third phase is PTO ferroelectric. However, due to the small amount of PFO at $x = 0.2$ and the presence of Fe^{3+} ions in two phases, a clear separation of these phases is not observed in the FORC diagrams.

However, the contour of the FORC diagram reveals a slightly larger dispersion of H_c , indicating the appearance of a second magnetic phase

with a lower coercive field than that of CFO. The observed increase in H_c (centered at approximately 5 kOe) due to nanostructuring, as shown in Fig. 9(b'', d''), can be attributed to the dispersion and size effects, observed during the mechanical activation of ferromagnetic compositions between Bridgman anvils [41,42]. The larger dispersion of coercive fields is likely due to two factors: a) the defective structure of mesoscopic-scale particles, which hinders the movement of domain walls and the rotation of magnetic moment vectors; and b) the formation of non-interacting single-domain particles during mechanical activation. The influence of stresses and grain size on hysteresis parameters and the ambiguity of their results have been previously discussed [43,44]. The behavior of non-interacting single-domain particles in FORC diagrams can be understood through the Preisach-Néel model [34,45].

A characteristic feature of the nanostructured samples resulting from mechanical activation is the presence of negative valleys in the field range $H_c = 2-8$ kOe (as seen in Fig. 9(b'', d'') and Fig. 10(b'', d'')). According to Ref. [37], this negative region corresponds to FORCs with a reversible field H_r , that is close to the coercive force H_c , where H_b is slightly larger than H_a . In this region, $\partial M / \partial H_b$ decreases with decreasing H_a , leading to a negative value of $\rho(H_a, H_b)$.

Nanostructuring of CFO by mechanical force led to an increase in the area of the hysteresis loop (see Fig. 9(b'')) and the formation of the FORC diagram with an intense horizontal ridge centered at $H_c = 4.75$ kOe. Along the axis of the interaction field H_u , the center of the ridge is shifted downward but remains higher than its position before mechanical activation. This FORC diagram corresponds to a nanostructured multi-domain structure. However, the crystal structure after mechanical activation is characterized by mechanical stresses induced by topological defects generated during the process. For each magnetic phase, there is a critical particle size at which the formation of magnetic domains becomes energetically unfavorable, causing the particles to become single-domain. In this state, changes in magnetization occur through the coherent rotation of spins, leading to an increase in the coercive force. A comparative analysis of particle size D and magnetic measurements indicates that a decrease in D results in an increase in the coercive field H_c . Additionally, structural defects contribute to the growth of H_c .

3.5. Magnetodielectric and magnetoresistive properties

Magnetodielectric and magnetoresistive effects are among the intriguing phenomena observed in multiferroics. The magnetodielectric effect involves a change in the dielectric constant caused by the

influence of a magnetic field on the ferroelectric component of the crystal lattice. Additionally, the influence of an electric field on magnetization can also be observed in these materials. When the magnetic and ferroelectric sublattices are not directly coupled within a composite material, the interaction between them can only occur indirectly. In composites, such effects often result from phenomena like magnetostriction or electrostriction. In our case, the CFO component exhibits negative magnetostriction, meaning it contracts in the presence of a magnetic field. Meanwhile, PTO, although ferroelastic, undergoes significant spontaneous deformation. Therefore, we do not expect any barriers to observing an indirect magnetic effect on the PTO component.

However, the partial substitution of the Ti^{4+} ions in $PbTiO_3$ with Fe^{3+} ions results in the formation of a third phase, a hexaferrite, which is multiferroic. In this phase, the magnetodielectric effect can be significantly enhanced. This substantial effect may be attributed to factors such as magnetostriction, the accumulation of charges at inhomogeneities, or interlayer polarization known as Maxwell-Wagner polarization [46]. In such cases, the magnetodielectric (MD) effect is considered to arise from an extrinsic mechanism.

If the dipole moment within a ferroelectric material changes under the influence of a magnetic field, it leads to a change in polarization that can be detected by observing the ferroelectric hysteresis loop $P(E)$. This

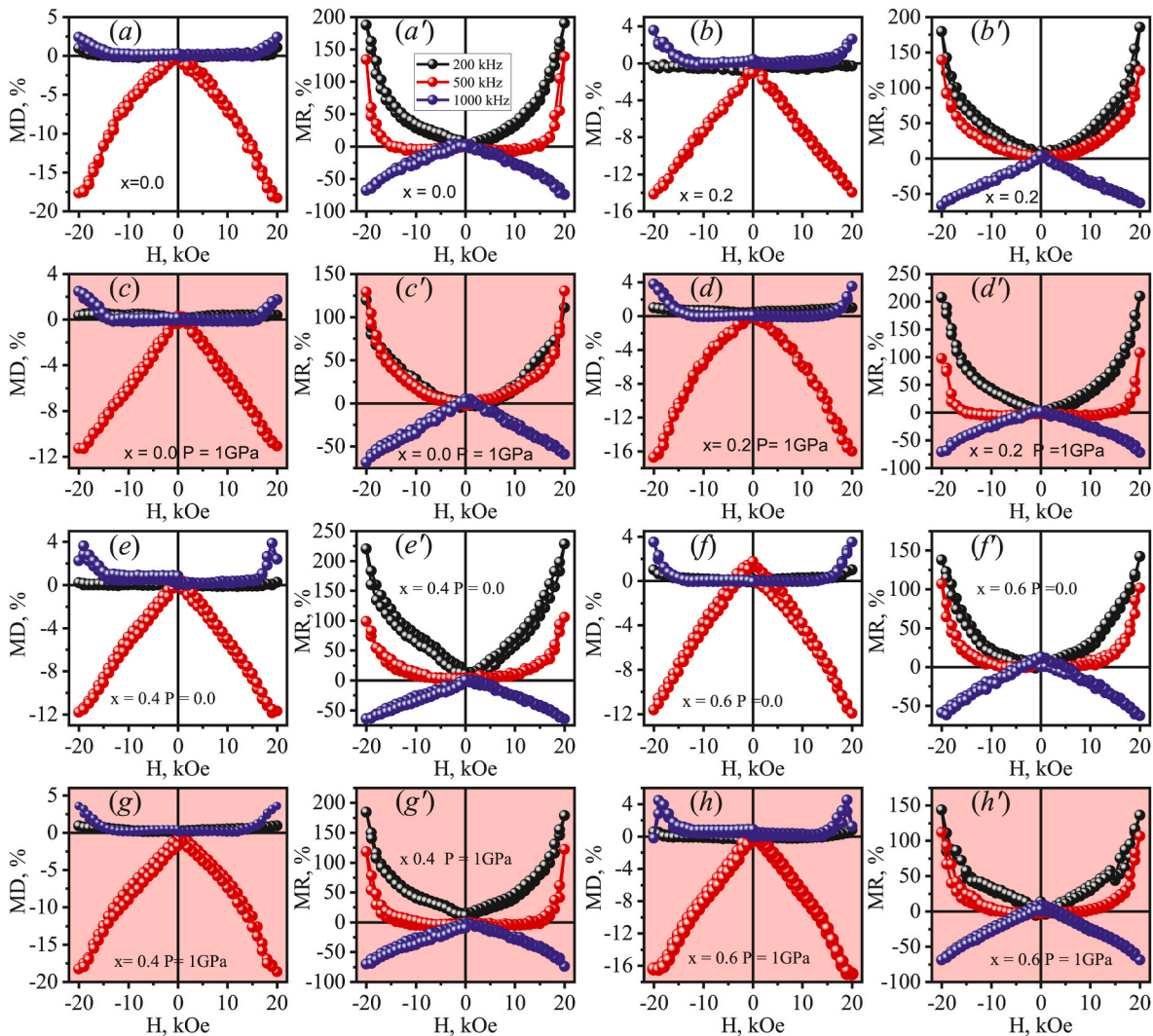


Fig. 11. Dependencies of $MD(B)$ and $MR(B)$ for $(1-x)CFO-xPTO$ compositions: Initial compositions are shown as $a(0.0)$, $a'(0.0)$, $b(0.2)$, $b'(0.2)$, $e(0.4)$, $e'(0.4)$, $f(0.6)$, $f'(0.6)$; nanostructured compositions are shown as $c(0.0)$, $c'(0.0)$, $d(0.2)$, $d'(0.2)$, $g(0.4)$, $g'(0.4)$, $h(0.6)$, $h'(0.6)$. Concentrations x are indicated in parentheses. Figures corresponding to nanostructured compositions are highlighted in red. (For interpretation of the references to colour in this figure legend, the reader is referred to the Web version of this article.)

indicates an internal source of magnetodielectric (*MD*) coupling [47]. However, after closely monitoring the ferroelectric hysteresis loop $P(E)$ with a magnetic induction change up to 2 T, no significant alteration in the loop's shape was observed. This suggests that the *MD* effect in our case is not due to internal coupling but is instead attributed to magnetoresistance and Maxwell-Wagner polarization. To measure the magnetodielectric $MD(B)$ and magnetoresistive $MR(B)$ coefficients, we used the following well-established formulas:

$$MD(B) = (\epsilon'(B) - \epsilon'(0)) / \epsilon'(0) \quad (8)$$

$$MR(B) = (\rho'(B) - \rho'(0)) / \rho'(0) \quad (9)$$

where ϵ' and ρ' denote the real parts of the dielectric constant and resistivity, respectively.

Fig. 11 shows the dependence of the $MD(B)$ and $MR(B)$ coefficients on the magnetic induction B , with the magnetic induction vectors \mathbf{B} and the electric field strength \mathbf{E} arranged orthogonally. A characteristic feature of the $MD(B)$ dependencies for all compositions is that, at measuring field frequencies of 200 and 1000 kHz, the behavior is nearly linear, with a positive deviation observed at the end of the magnetic field range at 1 MHz. At these frequencies, the $MD(B)$ coefficients do not exceed 4 %. In contrast, at a frequency of 500 kHz, the $MD(B)$ values are negative and exhibit a variation of 12–18 %, depending on the concentration x . Importantly, all graphs are nearly symmetrical relative to the zero lines, indicating minimal hysteresis.

The sign of $MR(B)$, as shown in Fig. 11, depends on the frequency of the measuring field. At frequencies of 200 kHz and 500 kHz, $MR(B)$ is positive and exhibits a parabolic dependence. At 1 MHz, however, $MR(B)$ becomes negative, with some compositions demonstrating a nearly linear dependence. This trend is consistent for both initial and nanostructured compositions. The positive $MR(B)$ coefficients range from 150 % to 225 %, depending on the concentration x , while the negative $MR(B)$ remains approximately 75 %, regardless of x .

As shown in Fig. 11, $(1-x)\text{CFO}-x\text{PTO}$ exhibits colossal magnetoresistance. As the magnetic field increases, the orientation of the spontaneous magnetization vector M_s changes, which affects spin-orbital interactions and crystal lattice parameters. This results in changes to the unit cell parameters of CFO, causing deformations in the crystal lattices of PTO and PFO.

The work done during magnetostrictive deformation of the sample corresponds to changes in the crystal field energies and spin-orbital interactions. Magnetostriction in CFO induces deformations in the crystal lattices of PTO and PFO, leading to increased scattering of charge carriers due to lattice vibrations. The coefficient $MR(B)$ shows a broader range of variation compared to $MD(B)$, and their signs depend on the frequency of the measuring field.

4. Conclusion

This study provides a comprehensive understanding of how physical properties in pre-synthesized $(1-x)\text{CFO}-x\text{PTO}$ composites can be manipulated by adjusting and nanostructuring component concentrations. By employing a top-down approach with uniaxial pressure using Bridgman anvils, we have effectively controlled these properties. The impedance formalism revealed that conductivity relaxation in $(1-x)\text{CFO}-x\text{PTO}$ composites deviates from Debye behavior, primarily due to Maxwell-Wagner polarization effects. Both before and after nanostructuring, the parameters R_g and R_{gb} of equivalent circuits showed classical temperature dependence, with R_{gb} consistently being greater than R_g in all nanostructured samples. The increase in capacitance (C_g and C_{gb}) with temperature is attributed to the enhanced mobility of charge carriers trapped in crystal lattice defects and the thermal expansion of the grain volume. The observed maxima are associated with Maxwell-Wagner polarization. Using FORC analysis, we demonstrated that the magnetic properties of $(1-x)\text{CFO}-x\text{PTO}$ composites

represented integral characteristics that enable the separation of contributions from each magnetic phase. The characteristics of these magnetic phases were found to depend on the size of the coherent scattering region D . The magnetoresistive coefficient $MR(B)$, showed a variation in the range of 150–250 %, depending on concentration x . The magnetodielectric effect was attributed to magnetostriction and interfacial polarization. Notably, adjusting the frequency of the measuring field allowed for the modification of the signs of both $MR(B)$ and $MD(B)$, demonstrating the dynamic control over these properties.

CRediT authorship contribution statement

Bashir Abdulvakhidov: Conceptualization. **Sadyk Sadykov:** Data curation. **Kamaludin Abdulvakhidov:** Writing – original draft. **Alexander Soldatov:** Funding acquisition. **Zhengyou Li:** Methodology. **Yury Rusalev:** Software. **Alexander Nazarenko:** Resources. **Pavel Plyaka:** Formal analysis. **Salim Otajonov:** Project administration. **Nurzod Yunusov:** Validation. **Maxamatjon Axmedov:** Writing – review & editing. **Marina Vitchenko:** Visualization. **Irina Mardasova:** Supervision.

Declaration of competing interest

The authors declare that they have no known competing financial interests or personal relationships that could have appeared to influence the work reported in this paper.

Acknowledgments

Research was financially supported by the Ministry of Science and Higher Education of the Russian Federation (State assignment in the field of scientific activity, No. FENW-2023-0019).

Appendix A. Supplementary data

Supplementary data to this article can be found online at <https://doi.org/10.1016/j.ceramint.2024.09.123>.

References

- [1] A.I. Gusev, A.A. Rempel, *Nanocrystalline Materials*, Cambridge International Science Publishing, 2004. <https://books.google.com.tr/books?id=kO8wzHV0xZOC>.
- [2] B. Abdulvakhidov, Z. Li, K. Abdulvakhidov, A. Soldatov, A. Nazarenko, B. Kulbuzhev, I. Mardasova, N. Lyanguzov, E. Sitalo, S. Sadykov, M. Sirota, I. Dmitrenko, A. Manukyan, Study of the structural-phase state and physical properties of $(1-x)(\text{CoFe}_2\text{O}_4)-x(\text{PbTiO}_3)$ compositions, *Appl. Phys. A* 128 (2022) 293, <https://doi.org/10.1007/s00339-022-05442-y>.
- [3] P.N. Vasambekar, C.B. Kolekar, A.S. Vaingankar, Magnetic behavior of Cd^{2+} and Cr^{3+} substituted cobalt ferrites, *Mater. Chem. Phys.* 60 (1999) 282–285, [https://doi.org/10.1016/S0254-0584\(99\)00062-0](https://doi.org/10.1016/S0254-0584(99)00062-0).
- [4] S.A. Paul, V.C. Mahajan, A.K. Ghatage, S.D. Lotke, S. Patil, V.C. Mahajan, A. K. Ghatage, S.D. Lotke, Structure and magnetic properties of Cd and Ti/Si substituted cobalt ferrites, *Mater. Chem. Phys.* 57 (1998) 86–91, [https://doi.org/10.1016/S0254-0584\(98\)00202-8](https://doi.org/10.1016/S0254-0584(98)00202-8).
- [5] P.A. Joy, S.K. Date, Effect of sample shape on the zero-field-cooled magnetization behavior: comparative studies on NiFe_2O_4 , CoFe_2O_4 and $\text{SrFe}_{12}\text{O}_{19}$, *J. Magn. Magn. Mater.* 222 (2000) 33–38, [https://doi.org/10.1016/S0304-8853\(00\)00572-2](https://doi.org/10.1016/S0304-8853(00)00572-2).
- [6] B.D. Cullity, C.D. Graham, *Ferrimagnetism*, in: *Introd. To Magn. Mater.*, John Wiley & Sons, Inc., Hoboken, NJ, USA, 2009, pp. 175–195, <https://doi.org/10.1002/9780470386323.ch6>.
- [7] B. Jaffe, W.R. Cook, H. Jaffe, Solid solutions of $\text{Pb}(\text{Ti}, \text{Zr}, \text{Sn}, \text{Hf})\text{O}_3$, in: *Piezoelectric Ceram.*, Elsevier, 1971, pp. 135–183, <https://doi.org/10.1016/B978-0-12-379550-2.50011-9>.
- [8] K. Okazaki, Developments in fabrication of piezoelectric ceramics, *Ferroelectrics* 41 (1982) 77–96, <https://doi.org/10.1080/00150198208210611>.
- [9] G.-L. Tan, M. Wang, Multiferroic $\text{PbFe}_{12}\text{O}_{19}$ ceramics, *J. Electroceram.* 26 (2011) 170–174, <https://doi.org/10.1007/s10832-011-9641-z>.
- [10] C.E. Ciomaga, M. Airimioaei, I. Turcan, A.V. Lukacs, S. Tascu, M. Grigoras, N. Lupu, J. Banya, L. Mitoseriu, Functional properties of percolative CoFe_2O_4 - PbTiO_3 composite ceramics, *J. Alloys Compd.* 775 (2019) 90–99, <https://doi.org/10.1016/j.jallcom.2018.10.088>.
- [11] G.D. Dwivedi, A.G. Joshi, H. Kevin, P. Shahi, A. Kumar, A.K. Ghosh, H.D. Yang, S. Chatterjee, Existence of the multiferroic property at room temperature in Ti

- doped CoFe_2O_4 , *Solid State Commun.* 152 (2012) 360–363, <https://doi.org/10.1016/j.ssc.2011.12.013>.
- [12] D. Ko, X.W. Zhao, K.M. Reddy, O.D. Restrepo, R. Mishra, T.R. Lemberger, I. S. Beloborodov, N. Trivedi, N.P. Padture, W. Windl, F.Y. Yang, E. Johnston-Halperin, Defect states and disorder in charge transport in semiconductor nanowires, *J. Appl. Phys.* 114 (2013), <https://doi.org/10.1063/1.4813494>.
- [13] K.G. Abdulvakhidov, M.A. Vitchenko, I.V. Mardasova, E.N. Oshaeva, Properties of the ferroelectric ceramics $\text{PbSc}_{0.5}\text{Ta}_{0.5}\text{O}_3$ fabricated from an ultradispersed powder, *Tech. Phys.* 53 (2008) 661–663, <https://doi.org/10.1134/S1063784208050228>.
- [14] K.G. Abdulvakhidov, E.N. Ubushaeva, I.V. Mardasova, M.A. Vitchenko, B. K. Abdulvakhidov, V.G. Zaletov, A.A. Amirov, I.K. Kamilov, A.S. Manukyan, P. S. Plyaka, G.B. Sukharina, Phase transitions, magnetic and dielectric properties of $\text{PbFe}_{0.5}\text{Nb}_{0.5}\text{O}_3$, *Ferroelectrics* 494 (2016) 182–191, <https://doi.org/10.1080/00150193.2016.1142749>.
- [15] E.N. Ubushaeva, K.G. Abdulvakhidov, I.V. Mardasova, B.K. Abdulvakhidov, M. A. Vitchenko, A.A. Amirov, A.B. Batdalov, A.G. Gamzatov, Nanostructured multiferroic $\text{PbFe}_{0.5}\text{Nb}_{0.5}\text{O}_3$ and its physical properties, *Tech. Phys.* 55 (2010) 1596–1599, <https://doi.org/10.1134/S1063784210110083>.
- [16] V. V. Boldyrev, Mechanochemistry and mechanical activation of solids, *Russ. Chem. Rev.* 75 (2006) 177–189, <https://doi.org/10.1070/RC2006v075n03ABEH001205>.
- [17] N.K. Evgenii Avvakumov, Mamoru Senna, *Soft Mechanochemical Synthesis*, Kluwer Academic Publishers, Boston, 2002, <https://doi.org/10.1007/b114163>.
- [18] E.G. Avvakumov, *Mechanical Methods of Activation of Chemical Processes*, 1986.
- [19] B.A. Tavger, V.Y. Demikhovskii, Quantum size effects in semiconducting and semimetallic films, *Sov. Phys. Usp.* 11 (1969) 644–658, <https://doi.org/10.1070/PU1969v011n05ABEH003739>.
- [20] A.L. Stroyuk, A.I. Kryukov, S.Y. Kuchmii, V.D. Pokhodenko, Quantum size effects in the photonics of semiconductor nanoparticles, *Theor. Exp. Chem.* 41 (2005) 67–91, <https://doi.org/10.1007/s11237-005-0025-9>.
- [21] T.A.S. Ferreira, J.C. Waerenborgh, M.H.R.M. Mendonça, M.R. Nunes, F.M. Costa, Structural and morphological characterization of FeCo_2O_4 and CoFe_2O_4 spinels prepared by a coprecipitation method, *Solid State Sci.* 5 (2003) 383–392, [https://doi.org/10.1016/S1293-2558\(03\)00011-6](https://doi.org/10.1016/S1293-2558(03)00011-6).
- [22] S.S. Cole, H. Espenschied, Lead titanate: crystal structure, temperature of formation, and specific gravity data, *J. Phys. Chem.* 41 (1937) 445–451, <https://doi.org/10.1021/j150381a009>.
- [23] W. Kraus, G. Nolze, POWDER CELL – a program for the representation and manipulation of crystal structures and calculation of the resulting X-ray powder patterns, *J. Appl. Crystallogr.* 29 (1996) 301–303, <https://doi.org/10.1107/S0021889895014920>.
- [24] V.I. Iveronova, G.P. Revkevich, *Theory of X-Ray Scattering/2nd Revised and Enlarged Edition*, Moscow Izd. Mosk. Univ. Pt, 1978.
- [25] R.W. (Reginald W. James, *The Optical Principles of the Diffraction of X-Rays*, Ox Bow Press, 1982. <https://cir.nii.ac.jp/crid/1130000796546654080>.
- [26] V.T. Bublik, A.N. Dubrovina, *Methods for studying the structure of semiconductors and metals*, Metall. Moscow. (1978).
- [27] J.R. Macdonald, Impedance spectroscopy, *Ann. Biomed. Eng.* 20 (1992) 289–305, <https://doi.org/10.1007/BF02368532>.
- [28] S. Wang, J. Zhang, O. Gharbi, V. Vivier, M. Gao, M.E. Orazem, Electrochemical impedance spectroscopy, *Nat. Rev. Methods Prim.* 1 (2021) 41, <https://doi.org/10.1038/s43586-021-00039-w>.
- [29] S. Parashar, S. Chaudhuri, S. Singh, M. Ghoranneviss, Electrical conduction in nanoceramic PGT synthesised by high energy ball milling, *J. Theor. Appl. Phys.* 7 (2013) 26, <https://doi.org/10.1186/2251-7235-7-26>.
- [30] S. Kumar, F. Ahmed, N.M. Shaalan, N. Arshi, S. Dalela, K.H. Chae, Investigations of structural, magnetic, and electrochemical properties of NiFe_2O_4 nanoparticles as electrode materials for supercapacitor applications, *Materials (Basel)* 16 (2023) 4328, <https://doi.org/10.3390/ma16124328>.
- [31] I.E. Geguzin, *The Diffusion zone*, Moscow Izd. Nauk, 1979.
- [32] Y.E. Geguzin, others, *Physics of Sintering*, 1984.
- [33] Z. Li, K. Abdulvakhidov, S. Soldatov, A. Soldatov, S. Otajonov, M. Axmedov, A. Nazarenko, P. Plyaka, B. Abdulvakhidov, V.J. Angadi, M. Sirota, A. Alshoek, I. Dmitrenko, Nanostructured $\text{YbMn}_{1-x}\text{Fe}_x\text{O}_3$ and its physical properties, *J. Mater. Sci. Mater. Electron.* 34 (2023) 1208, <https://doi.org/10.1007/s10854-023-10657-7>.
- [34] F. Preisach, Über die magnetische Nachwirkung, *Zeitschrift Fur Phys.* 94 (1935) 277–302, <https://doi.org/10.1007/BF01349418>.
- [35] A. Stancu, C. Pike, L. Stoleriu, P. Postolache, D. Cimpoesu, Micromagnetic and Preisach analysis of the first order reversal curves (FORC) diagram, *J. Appl. Phys.* 93 (2003) 6620–6622, <https://doi.org/10.1063/1.1557656>.
- [36] C. Carvallo, Ö. Özdemir, D.J. Dunlop, First-order reversal curve (FORC) diagrams of elongated single-domain grains at high and low temperatures, *J. Geophys. Res. Solid Earth* 109 (2004), <https://doi.org/10.1029/2003JB002539>.
- [37] A. Muxworthy, W. Williams, Magnetostatic interaction fields in first-order-reversal-curve diagrams, *J. Appl. Phys.* 97 (2005), <https://doi.org/10.1063/1.1861518>.
- [38] K. Heydaryan, M. Almasi Kashi, Characterization and magnetic properties of CoFe_2O_4 nanoparticles synthesized under gas atmosphere: effect of ferrofluid concentration on hyperthermia properties, *Adv. Ceram. Prog.* 9 (2023) 45–52, <https://doi.org/10.30501/acp.2023.402618.1126>.
- [39] R. Egli, VARIFORC: an optimized protocol for calculating non-regular first-order reversal curve (FORC) diagrams, *Global Planet. Change* 110 (2013) 302–320, <https://doi.org/10.1016/j.gloplacha.2013.08.003>.
- [40] I.D. Mayergoyz, Hysteresis models from the mathematical and control theory points of view, *J. Appl. Phys.* 57 (1985) 3803–3805, <https://doi.org/10.1063/1.334925>.
- [41] M.A. Sirota, K.G. Abdulvakhidov, A.P. Budnyk, A.V. Soldatov, A.L. Bugaev, T. A. Lastovina, Y.V. Kabirov, M.I. Mazuritskiy, P.S. Plyaka, S.N. Kallaev, Z. M. Omarov, S.A. Sadykov, B.K. Abdulvakhidov, I.V. Mardasova, M.A. Vitchenko, Mechanical activation and physical properties of $\text{Pb}(\text{Zr}_{0.56}\text{Ti}_{0.44})\text{O}_3$, *Ferroelectrics* 526 (2018) 1–8, <https://doi.org/10.1080/00150193.2018.1456130>.
- [42] K.G. Abdulvakhidov, M.A. Sirota, A.P. Budnyk, T.A. Lastovina, B. K. Abdulvakhidov, S.A. Sadykov, P.S. Plyaka, A.V. Soldatov, The role of defects in the physical properties of mechanically activated PbTiO_3 ferroelectrics, *J. Phys. Condens. Matter* 31 (2019) 135402, <https://doi.org/10.1088/1361-648X/aafebe>.
- [43] Y. Yu, D.J. Dunlop, Ö. Özdemir, Partial anhysteretic remanent magnetization in magnetite 1. Additivity, *J. Geophys. Res. Solid Earth* 107 (2002), <https://doi.org/10.1029/2001JB001249>.
- [44] C. Carvallo, A.R. Muxworthy, D.J. Dunlop, W. Williams, Micromagnetic modeling of first-order reversal curve (FORC) diagrams for single-domain and pseudo-single-domain magnetite, *Earth Planet Sci. Lett.* 213 (2003) 375–390, [https://doi.org/10.1016/S0012-821X\(03\)00320-0](https://doi.org/10.1016/S0012-821X(03)00320-0).
- [45] L. Néel, Remarques sur la théorie des propriétés magnétiques des couches minces et des grains fins, *J. Phys. Radium* 17 (1956) 250–255, <https://doi.org/10.1051/jphysrad:01956001703025000>.
- [46] G. Catalan, Magnetocapacitance without magnetoelectric coupling, *Appl. Phys. Lett.* 88 (2006) 102902, <https://doi.org/10.1063/1.2177543>.
- [47] Y. Tokura, S. Seki, Multiferroics with spiral spin orders, *Adv. Mater.* 22 (2010) 1554–1565, <https://doi.org/10.1002/adma.200901961>.